



Extended far-UV emission surrounding asymptotic giant branch stars as seen by GALEX


Downloaded from: <https://research.chalmers.se>, 2025-12-08 23:25 UTC

Citation for the original published paper (version of record):

Răstău, V., Mecina, M., Kerschbaum, F. et al (2023). Extended far-UV emission surrounding asymptotic giant branch stars as seen by GALEX. *Astronomy and Astrophysics*, 680.
<http://dx.doi.org/10.1051/0004-6361/202346120>

N.B. When citing this work, cite the original published paper.

Extended far-UV emission surrounding asymptotic giant branch stars as seen by GALEX

V. Răstău¹ , M. Mečina¹, F. Kerschbaum¹, H. Olofsson², M. Maercker², M. Drechsler³, X. Strottner⁴, and L. Mulato⁵

¹ Department of Astrophysics, University of Vienna, Türkenschanzstrasse 17, 1180 Vienna, Austria
e-mail: vlad.rastau@univie.ac.at

² Department of Space, Earth and Environment, Chalmers University of Technology, Onsala Space Observatory, 439 92 Onsala, Sweden

³ Sternwarte Bärenstein, Feldstraße 17, 09471 Bärenstein, Germany

⁴ Équipe StDr, Montfraise, 01370 Saint-Étienne-du-Bois, France

⁵ 2SPOT (Southern Spectroscopic Observatory Team), 45 Chemin du Lac, 38690 Châbons, France

Received 10 February 2023 / Accepted 25 September 2023

ABSTRACT

Aims. Our goal is to study the long-term mass-loss rate characteristics of asymptotic giant branch (AGB) stars through wind–wind and wind–interstellar medium interaction.

Methods. Far-ultraviolet (FUV) images from the GALEX survey are used to investigate extended UV emission associated with AGB stars.

Results. FUV emission was found towards eight objects. The emission displays different shapes and sizes; interaction regions were identified, often with infrared counterparts, but no equivalent near-ultraviolet (NUV) emission was found in most cases.

Conclusions. The FUV emission is likely attributed to shock-excited molecular hydrogen, considering the lack of NUV emission and the large space velocities of the objects, and makes it possible to trace old structures that are too faint to be observed, for instance, in the infrared.

Key words. stars: AGB and post-AGB – stars: mass-loss – stars: winds, outflows – ultraviolet: stars

1. Introduction

The asymptotic giant branch (AGB) phase is the last evolutionary stage of low- to intermediate-mass stars ($0.8 < M < 8 M_{\odot}$) before they become white dwarfs (Herwig 2005). Subject to strong convective dredge-up and slow but pronounced dusty winds, AGB stars are major contributors to the enrichment of the interstellar medium (ISM; Schneider et al. 2014). Understanding how the above combination impacts their lifetimes is therefore crucial to our understanding of both stellar evolution and galactic-scale changes.

The mass-loss (ML) process of AGB stars is normally viewed as a slow and continuous wind (Höfner & Olofsson 2018) that is responsible for the formation of extended dust and gas structures around such circumstellar envelopes (CSEs). However, more evidence has emerged in support of more complex scenarios regarding the overall ML process, and that of the formation of extended features (Maercker et al. 2012; Cox et al. 2012; Decin et al. 2020). For example, the strong thermal pulses that occur in this evolutionary phase produce fast and high ML winds, which then collide with the slower interpulse winds. A shock develops, following this wind–wind interaction, which can also create large structures around AGB stars (i.e. geometrically thin shells, filaments, and clumps). Analysing the morphology of extended features can reveal information about the ML process and the central object, as it did for example in the case of R Sculptoris (Maercker et al. 2012). Cox et al. (2012) performed an infrared morphological analysis of a large sample of AGB stars showing extended emission, and divided the extended structures into four main categories based on their shape: fermata

(large arcs), eyes (concentric arcs), rings (circular structures), and irregular (for diffuse structures or any structures that do not fall into the previous categories). Our discussion here follows this classification.

To date only a handful of AGB stars showing extended emission in the ultraviolet (UV) have been studied, the most famous one being Mira (see Martin et al. 2007). Along with the features found around CW Leo and RW LMi (see Sahai & Chronopoulos 2010; Sahai & Mack-Crane 2014) these are fine examples of wind–ISM interaction. Recently, Sanchez et al. (2015) detected, for the first time, UV emission cospatial with a detached dust shell previously found in the infrared (IR), which was attributed to outflow and/or ISM shocks. All in all, not much is known about AGB winds in this wavelength regime. Therefore, in the scope of this project our aim is to expand the sample of AGB stars that display extended UV emission, more specifically far-UV (FUV) emission ($0.13\text{--}0.18 \mu\text{m}$) taken from the GALEX catalogue. In Sect. 2 we briefly describe the sample and the various methods used. A more detailed analysis is provided for each object in Sect. 3, while Sect. 4 is reserved for the discussion of our results and the conclusions we draw from them.

2. Sample and method

2.1. Sample

This study focuses on a small sample of AGB stars that show extended FUV emission ($0.13\text{--}0.18 \mu\text{m}$) in the GALEX catalogue (Bianchi et al. 2017). The sample was obtained following

Table 1. Stellar parameters.

	RA	Dec	π [mas]	Distance [pc]	T_{eff} [K]	L [L_{\odot}]	P [days]	\dot{M} [$M_{\odot} \text{ yr}^{-1}$]	Var type	Spectral type
U Ant	10 ^h 35 ^m 12.85 ^s	−39°33′45.32″	3.4 ^(a)	294 ^(a)	2300 ^(d)	4500 ^(d)	—	4.0×10^{-8} ^(m)	Lb	C-N3
R Dor	04 ^h 36 ^m 45.59 ^s	−62°04′37.79″	22.7 ^(a)	44 ^(a)	2710 ^(e)	2800 ^(e)	223 ^(k)	1.6×10^{-7} ⁽ⁿ⁾	SRb	M8III:e
β Gru	22 ^h 42 ^m 40.05 ^s	−46°53′04.47″	18.4 ^(b)	54	3480 ^(f,g)	2500 ^(f)	37 ^(k)	1.0×10^{-9}	SRb	M4.5III
W Hya	13 ^h 49 ^m 02.00 ^s	−28°22′03.53″	11.0 ^(a)	87 ^(a)	2600 ^(h)	4730 ^(h)	390 ^(l)	1.5×10^{-7} ^(o)	SRa	M7.5-9e
TV Psc	00 ^h 28 ^m 02.91 ^s	+17°53′35.25″	6.0 ^(c)	167	3500 ^(*)	2500 ^(*)	49 ^(k)	1.0×10^{-8}	SR	M3III
RZ Sgr	20 ^h 15 ^m 28.40 ^s	−44°24′37.47″	2.3 ^(a)	432 ^(a)	2400 ⁽ⁱ⁾	5000 ^(j)	172 / 338 ^(k)	3.0×10^{-6} ^(p)	M	S4,4ep
DM Tuc	22 ^h 57 ^m 05.85 ^s	−57°24′04.22″	4.3 ^(c)	230	2700 ^(*)	3340 ^(j)	75 / 145 ^(k)	4.1×10^{-7} ^(j)	SRb	M8III
V420 Vul	20 ^h 59 ^m 36.83 ^s	+26°28′34.42″	0.4 ^(c)	2429	3000 ^(*)	4000 ^(*)	377 ^(k)	1.7×10^{-7}	M	N:e

Notes. Due to a lack of literature data, the luminosity and effective temperature values flagged with asterisks (*) were calculated by us using the radiative transfer code *More of DUSTY* (Groenewegen 2012). The luminosities for U Ant, RZ Sgr, R Dor, and W Hya were scaled based on the results of the various works referenced in this table and the distances derived by Andriantsaralaza et al. (2022).

References. ^(a)Andriantsaralaza et al. (2022); ^(b)van Leeuwen (2007); ^(c)Gaia Collaboration (2022); ^(d)Maercker et al. (2018); ^(e)Ohnaka et al. (2019); ^(f)Judge (1986); ^(g)Engelke et al. (2006); ^(h)Ramstedt & Olofsson (2014); ⁽ⁱ⁾Schöier et al. (2013); ^(j)Winters et al. (2003); ^(k)Samus’ et al. (2017); ^(l)Vogt et al. (2016); ^(m)Kerschbaum et al. (2017); ⁽ⁿ⁾Maercker et al. (2016); ^(o)Khouri et al. (2014); ^(p)Ramstedt et al. (2009).

a systematic inspection by eye of GALEX FUV images, carried out via Aladin on the full-sky survey (GALEX GR6/7 FUV / GR6 AIS FUV), with the scope of finding previously unreported sources that display faint extended emission in this wavelength regime, regardless of source type. Any detections were correlated with several catalogues, and those that were associated with known objects were flagged. Here we report on newly found emission associated with variable stars of Mira-type, Semiregular or Irregular (M, SRa, SRb, SR, or Lb), that are listed in the General Catalogue of Variable Stars (GCVS; Samus’ et al. 2017). Other results, for example on supernova remnants, can be found in Fesen et al. (2021) or Kimeswenger et al. (2021). Using the GCVS in the identification process introduces a bias towards AGB stars which are more optically bright and are located towards the low end of the ML spectrum. Our object list consists of five M-type stars (oxygen-rich, C/O < 1), two C-type stars (carbon-rich, C/O > 1), and one S-type star (C/O \approx 1). The stars along with their basic parameters (gathered from the literature where available) are described in Table 1. The distances used here are from Andriantsaralaza et al. (2022), derived from the *Gaia* DR3 parallaxes (Gaia Collaboration 2022), or derived from the HIPPARCOS parallaxes (van Leeuwen 2007) for the cases where *Gaia* measurements were not available. Only three objects have a renormalised unit weight error (RUWE) for their *Gaia* measurements (see Table 2). One of them (TV Psc) has a value that would indicate somewhat poor quality, but since the measurements were not that far off from previous estimates we decided to keep the values from *Gaia* DR3. We adopted CO mass-loss rates (MLRs) from the literature where available and for the remaining cases we estimated the present-day MLR via spectral energy distribution (SED) fitting done with the *More of DUSTY* code (with an assumed gas-to-dust mass ratio of 200; Groenewegen 2012). The fitting was done using model spectra (Aringer et al. 2016, 2019) and the gathered stellar parameters (Table 1).

2.2. UV data

The FUV (bandpass 1344–1786 Å) and near-ultraviolet (NUV, bandpass 1771–2831 Å) data used in this study come from pipeline-calibrated images (in units of counts per second per

Table 2. Stellar motion data.

	pm_{RA} [mas yr ^{−1}]	pm_{Dec} [mas yr ^{−1}]	RUWE	r_v [km s ^{−1}]	V_{lsr} [km s ^{−1}]
U Ant	−31.5 ^(a)	2.6 ^(a)	—	41 ^(d)	42
R Dor	−69.4 ^(b)	−75.8 ^(b)	—	26.1 ^(d)	40
β Gru	135.2 ^(b)	−4.4 ^(b)	—	−0.3 ^(d)	20
W Hya	−51.8 ^(c)	−59.7 ^(c)	—	42.3 ^(d)	50
TV Psc	114.6 ^(a)	20.3 ^(a)	2.4404 ^(a)	5.31 ^(e)	78
RZ Sgr	15.5 ^(a)	−10.9 ^(a)	—	−38.25 ^(a)	41
DM Tuc	65.8 ^(a)	−55.9 ^(a)	1.1879 ^(a)	−35.5 ^(f)	87
V420 Vul	−9.4 ^(a)	−4.1 ^(a)	1.8602 ^(a)	14.9 ^(a)	132

Notes. Proper motions (pm_{RA} , pm_{Dec}), *Gaia* renormalised unit weight error (RUWE), radial velocity (r_v) and space velocity with respect to the local standard of rest (V_{lsr} , LSR transformation based on Schönrich et al. 2010).

References. ^(a)Gaia Collaboration (2022); ^(b)van Leeuwen (2007); ^(c)Gaia Collaboration (2018); ^(d)Gontcharov (2006); ^(e)Famaey et al. (2009). ^(f)The value is based on the result of Winters et al. (2003) and the LSR transformation of Schönrich et al. (2010).

pixel) retrieved from the GALEX archive, GR6/7¹, with a 1.2 degree field of view, a pixel scale of 1.5″, and a FWHM angular resolution of 4″ (FUV) and 5.6″ (NUV). Table 3 lists the exposure times of the retrieved images. The emission detected around each star is displayed in Fig. 1 and throughout Sect. 3. We also performed some basic FUV flux density estimations for the extended structures (with flux densities obtained via a conversion of the photon counts; see Appendix A), the values being listed in Table 4 along with their estimated sizes. The size measurements are based on the absolute distances and the apparent angular sizes of the objects, while the age determination of the extended structures also includes the assumption of a constant expansion velocity of 10 km s^{−1} or other values in those cases where more accurate velocity measurements are available.

¹ The data are from <https://galex.stsci.edu/GR6/>. U Ant data were calibrated using the GR7 pipeline (http://www.galex.caltech.edu/wiki/Public:Documentation/Chapter_8), while the image data for the rest of the objects were calibrated with the GR6 pipeline (https://galex.stsci.edu/Doc/GI_Doc_Ops7.pdf).

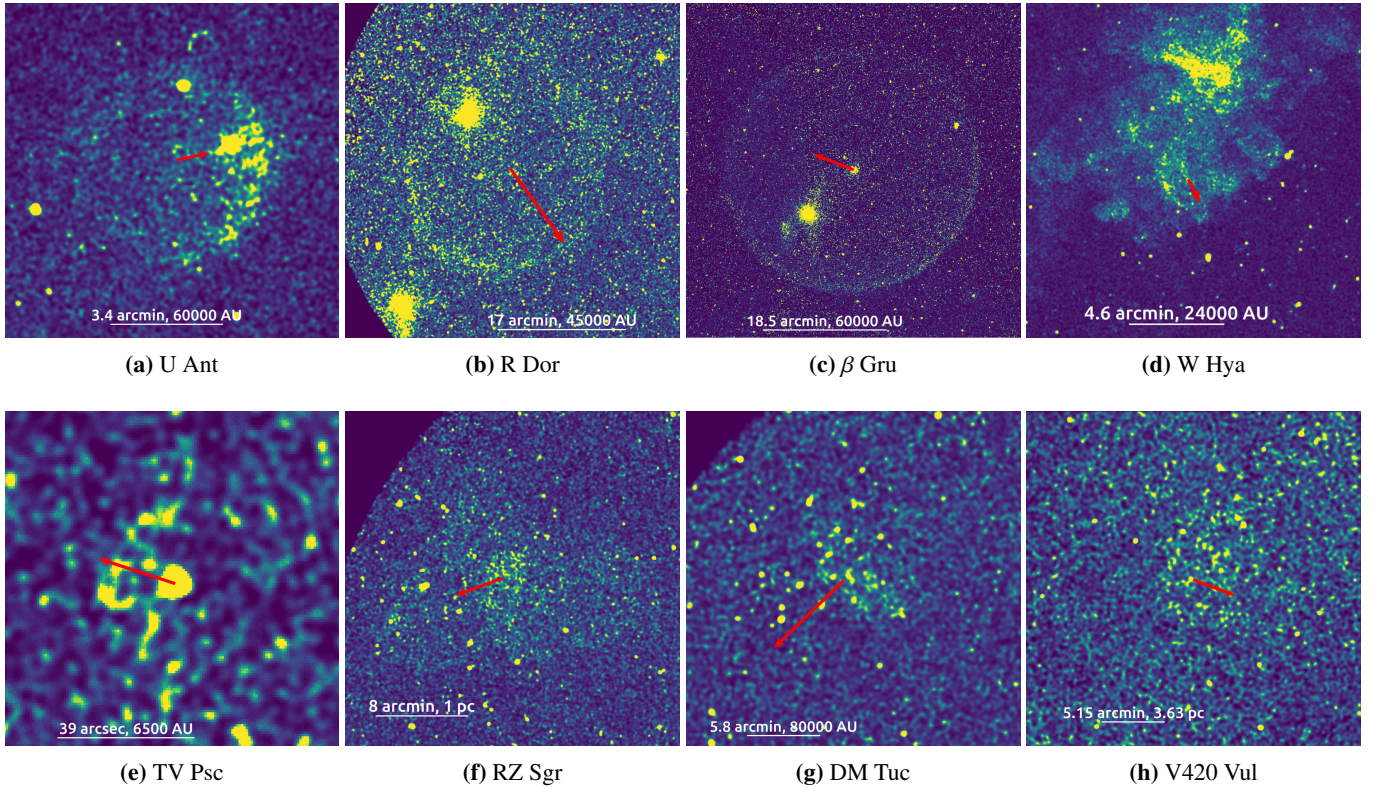


Fig. 1. GALEX catalogue FUV images of the stars and their surroundings. North is up and east to the left; the same orientation is used for all the images. The arrows (originating at the location of each star) represent the projected distance the stars would travel over a timescale of 5000 yr, with the exception of TV Psc (where the distance corresponds to 500 yr), RZ Sgr (40 000 yr), and V420 Vul (20 000 yr). The space motion vector indicates the velocity relative to the local standard of rest (LSR; Schönrich et al. 2010) and is derived from proper motion and radial velocity data using the Astropy coordinates package. The large bright spots seen in the images for β Gru, R Dor, and U Ant come from objects along the line of sight, either background stars or galaxies.

Table 3. GALEX observations.

	Exposure time [s]		Observation date
	NUV	FUV	
U Ant	6379	1119	7,11 Apr. 2009
R Dor	206	206	28 Sep. 2008
β Gru	199, 215, 244	199, 215, 244	8 Aug. 2007
W Hya	4420	4420	16 May 2009
TV Psc	460	339	28 Oct. 2003, 26 Sep. 2004
RZ Sgr	210	210	4 Jul. 2007
DM Tuc	385	320	9 Aug. 2003
V420 Vul	398	255	30 Jun. 2004

Notes. Exposure times and observation dates of the GALEX data used for this study (GALEX archive – GR 6/7).

As can be clearly seen, the FUV emission produces various types of structures, from well-defined rings (β Gru, R Dor) to faint arcs (eye, fermata: TV Psc, W Hya, U Ant), and to fuzzy faint blobs (irregular: DM Tuc, RZ Sgr, V420 Vul). One important aspect is that no near-UV (NUV, 0.17–0.30 μ m) counterpart was detected for most structures. The exceptions are TV Psc, which displays some stronger NUV emission around the star, and RZ Sgr. As discussed in previous studies (Martin et al. 2007; Sahai & Chronopoulos 2010; Sahai & Mack-Crane 2014) the presence of FUV emission combined with the lack of NUV emission is indicative of the origin of the FUV flux.

Table 4. Results on the extended emission.

	F_{ex} [mJy]	F_{fuv} [mJy]	R_{es} [AU]	t_{kin} [yrs]
U Ant	1.3	–	50 000	23 700
R Dor	12.7	–	37 000	17 500
β Gru	9.7	3.83	58 000	27 500
W Hya	0.6	–	6 250	3 000
TV Psc	0.07	0.174	6 600	3 100
RZ Sgr	1.6 ^(*)	–	180 000	85 000
DM Tuc	1.1	3.53×10^{-3}	10 000	–
V420 Vul	3.7	–	–	–

Notes. FUV flux densities (F_{ex}), radius (R_{es}), and kinematic age (t_{kin}) of the extended structures presented in Sect. 3. F_{fuv} is the GALEX FUV flux of the stars (Bianchi et al. 2017). We assumed an expansion velocity of the outflow of 10 km s^{−1} for all objects. ^(*) The FUV flux density of RZ Sgr used here corresponds only to the inner, more pronounced, emission.

One cause could be wind–ISM interaction, where the emission is attributed to shocked molecular hydrogen, which does not emit in the NUV. Sanchez et al. (2015) argue that if enough H₂ molecules survive dissociation by the interstellar radiation field, this could show up as clumps of emission in the FUV regime. The FUV data were also compared to far-infrared (FIR) pipeline-calibrated images from the *Herschel* or Akari surveys. The FUV

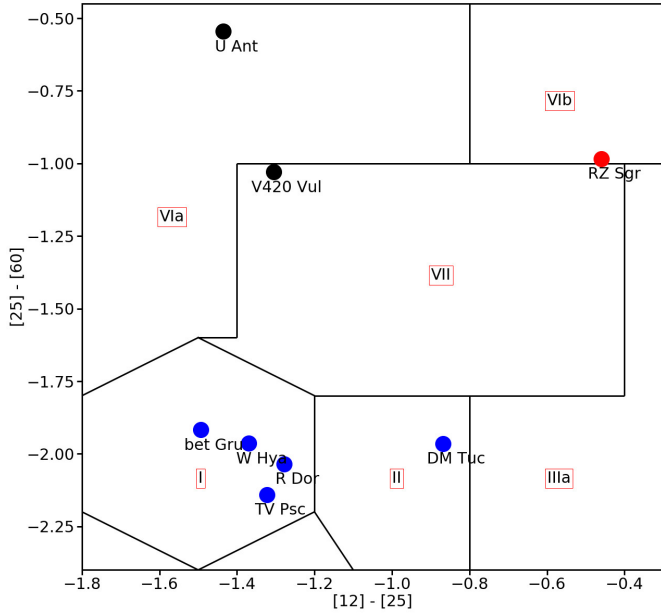


Fig. 2. IRAS colour-colour diagram (van der Veen & Habing 1988). The objects are colour-coded as follows: blue dots for M-type stars, red dots for S-type stars, and black dots for C-type stars.

emission was found to be cospatial with IR emission, with possible implications being discussed in the following sections.

Using infrared photometric data, we plotted the objects in an IRAS colour-colour diagram (see Fig. 2), which was introduced by van der Veen & Habing (1988) to illustrate the evolution of O-rich AGB stars with circumstellar envelopes (CSEs). The different regions denoted by roman numerals lay out the evolutionary sequence as follows: it begins with mostly non-variable early-AGB stars (M-type) that show no evidence of having a CSE (region I), continues through regions II–IV as the stars increase in variability and ML and start developing thicker O-rich CSEs, and ends in regions IV and V where AGB stars that are close to the end of the ML process and those that have reached the planetary nebula stage are found. Regions VI and VII in the diagram contain C- and S-type AGB stars, objects that have seen a shift towards a more C-rich chemistry via dredge-up events caused by thermal pulses, with similar variability and CSE characteristics seen in regions II and III. Finally, group VIII represents outliers and extreme cases of objects seen towards the end of AGB evolution (i.e. objects from regions IV and V). The objects in our sample seem to end up in the expected categories, with the M-type stars in groups specific for stars with no or tenuous CSEs. The C-type stars in the sample ended up in categories containing objects with C-rich CSEs. The S-type star is located where objects that might experience episodic ML are expected, having a colder dust component that could be located further away from the object.

2.3. CO line observations for β Gruis

The star β Gru is the only object that clearly shows an essentially circular FUV shell centred on the star. This warranted an attempt to study the mass-loss history of the object using CO rotational line emission. Observations of the CO($J=2-1$) line were obtained using the APEX telescope (Güsten et al. 2006) in April 2022. No CO($J=2-1$) emission was detected, having achieved an upper limit of 1 mK for the rms noise level (in main

beam brightness scale; beam width = $27''$) at a velocity resolution of 2 km s^{-1} .

3. Object analysis

3.1. *U Antilae*

U Ant is a C-type irregular variable located 294 pc away. Based on its effective temperature and luminosity, $T_{\text{eff}} = 2300 \text{ K}$ and $L = 4500 L_{\odot}$ (Maercker et al. 2018), it is a relatively evolved AGB star. A low present-day MLR, $4 \times 10^{-8} M_{\odot} \text{ yr}^{-1}$, has been estimated using CO line data (Kerschbaum et al. 2017); the rough estimate we computed is of the same order of magnitude.

The circumstellar environment of U Ant has been well studied. A first detection of an overall spherically symmetric detached CO shell around the star was reported by Olofsson et al. (1988). The CO shell emission, located at a distance of about $43''$, has been imaged in detail using ALMA (Kerschbaum et al. 2017). The studies of Maercker et al. (2010) and Kerschbaum et al. (2011) detected a dust shell counterpart to the CO shell in dust-scattered light and infrared dust emission (see Fig. 3b), respectively. This detached shell most likely originates from a short period of high ML that the star underwent about 2700 yr ago, when the MLR could have been as high as $10^{-5} M_{\odot} \text{ yr}^{-1}$. This shell is not visible in the UV range.

In a study based on IRAS $100 \mu\text{m}$ observations, Izumiura et al. (1997) reported the detection of a larger dust shell with a radius of $\approx 3'$, about four times larger than the inner CO shell. At low levels, the *Herschel* PACS $160 \mu\text{m}$ image confirms the structure reported by Izumiura et al. (1997; Fig. 3b), but the IR emission is quite diffuse so it is hard to tell what its full extent is. However, this outer shell is clearly seen in the FUV image (Fig. 3a) marked by the cyan circle that has a radius of $3'$ (a similar size was deduced in a recently published independent study by Sahai & Stenger 2023). With an increased intensity in the direction of motion of the star, the FUV emission resembles a bow shock and is located at a distance of about 50 000 AU. Assuming an expansion velocity of 10 km s^{-1} the kinematic age of the shell would be $t_{\text{kin}} \approx 23\,700 \text{ yr}$. Considering the correlation between the direction of motion of the star, the space velocity (42 km s^{-1}) and the emission intensity in the FUV, this structure is most likely caused by wind-ISM interaction.

3.2. *R Doradus*

R Dor is a relatively evolved M-type SRb variable star located only 44 pc away, with a $T_{\text{eff}} \approx 2700 \text{ K}$ (Ohnaka et al. 2019) and a luminosity of about $2800 L_{\odot}$ (Ohnaka et al. 2019). Two periods have been reported for this object (172 or 338 days). Bedding et al. (1998) suggested that the star oscillates between two different pulsation modes (first and third overtone).

R Dor's position in the IRAS colour-colour diagram (Fig. 2) suggests that it has a tenuous CSE. This star is rather well-studied in CO line emission, and its MLR has been reliably estimated to be of the order of $10^{-7} M_{\odot} \text{ yr}^{-1}$ (Maercker et al. 2016; Andriantsaralaza et al. 2021; our estimate for its present-day MLR, see Table 1, is in agreement with this value). High-angular-resolution molecular line studies suggest that R Dor has a low-mass close-in companion, and that this may have an effect on the structure of its CSE, at least on the inner parts (Vlemmings et al. 2018).

The emission seen in the FUV is largely circular and has no NUV counterpart. The same extended structure can be seen in the FIR (see Fig. 4), although not as pronounced. With

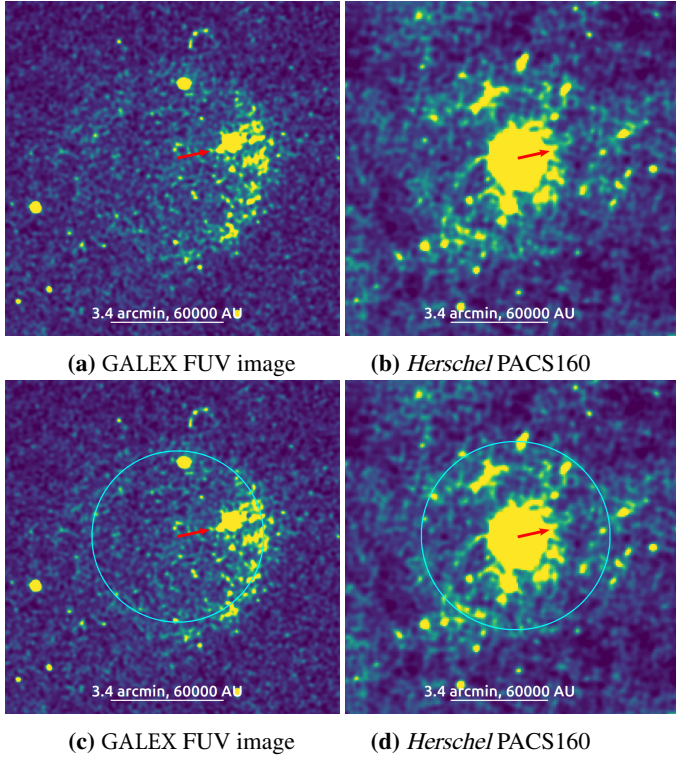


Fig. 3. Extended emission seen around U Ant in FUV (left) and FIR (right, in units of Jy pixel^{-1}). While the central FIR emission present close to the star is not visible in the FUV, the larger arc located further away from the star is present in both images and is tentatively marked by the cyan dashed circle (radius of $3'$). The arrows are the same as in Fig. 1.

some tentative asymmetry towards the north in the FUV image (Fig. 4a), this ring structure has a radius of $R_{\text{es}} \approx 37\,000$ AU ($13.5'$, indicated by the dashed ellipse in Fig. 4). This result is in agreement with an analysis recently published in parallel by Ortiz & Guerrero (2023). Assuming a gas expansion velocity of 10 km s^{-1} , the kinematic age of this structure would be $\approx 17\,500$ yr. Following its fairly circular shape and the lack of NUV emission, this extended structure may be caused by shocked H_2 gas, be it wind–ISM or wind–wind interaction. The shock hypothesis could be supported by the fact that the space velocity of the star is a few times higher than the expansion velocity of its wind ($v_{\text{slr}} = 40$ vs. 10 km s^{-1}). The seemingly stronger emission in other directions than that of the star’s proper motion could be caused by H_2 clumps (as postulated by Sanchez et al. 2015), although the short exposure time is not sufficient to fully reveal whether this is the case or not. The clumpy aspect is slightly more evident in the FIR images (Fig. 4b).

3.3. β Gruis

β Gru is located only 54 pc away (from HIPPARCOS parallax). Considered a SRb variable, its parameters gathered from the literature indicate an early-type AGB star, having an effective temperature $T_{\text{eff}} = 3480\text{ K}$ (Engelke et al. 2006), a luminosity of $L = 2500 L_{\odot}$ (Judge 1986), and a pulsation period $P = 37$ days (Otero & Moon 2006).

Using various UV emission lines (e.g. Si I, Si II, C I, Fe II) originating in the outer atmosphere, the study of Judge (1986) set a lower limit of $5 \times 10^{-9} M_{\odot} \text{ yr}^{-1}$ for the MLR of the star. Using the obtained upper limit to the $\text{CO}(J=2-1)$ line and the

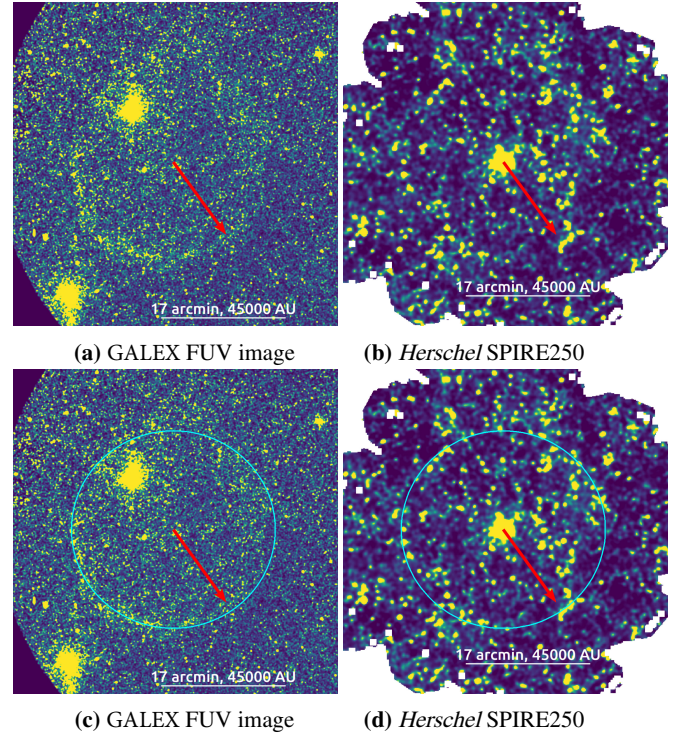


Fig. 4. Extended emission seen around R Dor in FUV (left) and IR (right). The cyan ellipse gives the approximate location of the extended structure. The arrows are the same as in Fig. 1. The bright spot seen NE of R Dor in the GALEX image is a hot subdwarf located about 1300 pc away.

MLR formula of Ramstedt et al. (2008), we obtain a crude upper limit to the gas-MLR of $10^{-9} M_{\odot} \text{ yr}^{-1}$ (a gas expansion velocity of 7 km s^{-1} and a circumstellar CO-to- H_2 abundance ratio of 4×10^{-4} were adopted). We note that the present-day ML that we computed via SED-fitting is consistent with this upper limit ($1.7 \times 10^{-9} M_{\odot} \text{ yr}^{-1}$). There is no indication of CO line emission from any detached shell.

Without substantial mass-loss, or with little to no dust emission (Sloan & Price 1998), and based on its placement in the IRAS colour–colour diagram (Fig. 2), β Gru appears to lack a CSE. However, recent radio observations show a potential departure from a black-body spectrum in the millimetre regime (Murphy et al. 2010; Everett et al. 2020). The presence of the essentially circular UV shell centred on the star (Fig. 1c) indicate that β Gru underwent a significant episode of ML earlier in its evolution. All of this, combined with the lack of NUV or IR emission, suggests the shell seen in the FUV images could be attributed to wind–ISM interaction. We note that there is a lack of correlation between the strength of the FUV emission and the space motion of the star, but the low exposure time of the image is not enough to reveal more than that (i.e. whether there are any clumps of emission). With a radius of $R_{\text{es}} \approx 58\,000$ AU of the UV shell, its kinematic age is $t_{\text{kin}} \approx 27\,500$ yr, assuming an expansion velocity of 10 km s^{-1} . Alternatively, the object is still on the RGB and the UV shell is an effect of RGB wind–ISM interaction.

3.4. W Hydrae

W Hya is one of the most evolved stars in our sample. It is an M-type SRa variable located about 87 pc away (Andriantsaralaza et al. 2022), and has an effective temperature of about 2600 K

(Massalkhi et al. 2020), a luminosity of $4730 L_{\odot}$ (scaled for the distance given by Andriantsaralaza et al. 2022), and a pulsation period of 390 days (Vogt et al. 2016).

The IRAS colour-colour diagram placement (Fig. 2) indicates that W Hya has no CSE, or a very thin CSE, but based on more recent studies and images there is a great deal of evidence that this is not true. The star has been studied extensively in the CO regime, and its present-day MLR is of the order of $10^{-7} M_{\odot} \text{ yr}^{-1}$ (Khouri et al. 2014; Ramstedt et al. 2020). The studies of Muller et al. (2008) and Vlemmings et al. (2011) have also detected the potential presence of a slow bipolar outflow, following $\text{HCN}(J=3-2)$ and $\text{SO}(J=5-4)$ observations. In a very recent study, combining ALMA observations of $^{12}\text{CO}(J=2-1)$ and $^{29}\text{SiO}(J=8-7)$ line emission and VLT visual and infrared observations, Hoai et al. (2022) postulate a two-component scenario for the CSE of W Hya. They found an approximately spherical shell, at about 30 AU from the star, that is stable on a timescale of hundreds of years and that has an expansion velocity of 5 km s^{-1} . They also present evidence for an elongated structure (10° west of north) which shows features characteristic of recent mass ejection; this component is found to be variable on a shorter timescale, years maybe even months. An older study by Hawkins (1990) suggested that W Hya might have previously experienced an episode of increased ML; this hypothesis is based on the fact that its present-day ML (measured at the time) was not high enough to justify the detection of an extended dust shell via IRAS observations.

The GALEX FUV image shows extended emission that seems to consist of two components. A fairly circular shell is found closer to the star and is cospatial with FIR emission detected by the *Herschel* Space Observatory (see Fig. 5), a result reported in a recent study by Sahai & Stenger (2023). With a radius of $R_{\text{es}} = 6250 \text{ AU}$ ($\approx 1'$) and an assumed gas expansion velocity of 10 km s^{-1} , the kinematic age of this shell corresponds to $\approx 3000 \text{ yr}$. No NUV emission is seen around W Hya and once again the FUV component appears weaker in the direction of the star's proper motion. Considering its relative proximity to the star this structure could be caused by wind-wind interactions. The bright spot visible in the eastern part of the structure is most likely caused by the star HD 120305, located 130 pc away (Gaia Collaboration 2022). The second and more ambiguous component consists of very fuzzy emission seen to the north-west with respect to the star (Figs. 5a,b). This emission is very pronounced in the FUV, but it is also visible in the FIR images where it is more reminiscent of a tail-like structure. There is no obvious correlation between the direction of motion of the star and the direction in which the irregular emission is present. It is also hard to tell if the variable elongated structure found by Hoai et al. (2022) north-west of the star could be in any way connected to this irregular FUV emission that extends to a distance beyond 24 000 AU from W Hya.

3.5. TV Piscium

TV Psc is an M-type SR variable located about 190 pc away, with a pulsation period of only 49 days (Samus' et al. 2017). Since it is not a well-studied object, literature data were not available regarding its luminosity, effective temperature, or MLR. Based on the effective temperature and luminosity we obtained by using the radiative transfer code *More of DUSTY* (Groenewegen 2012), it falls in the same early-type AGB category as β Gru (having a similar T_{eff} and L). The present-day MLR we computed, $1.5 \times 10^{-8} M_{\odot} \text{ yr}^{-1}$, also puts it at the low end of the AGB ML characteristics.

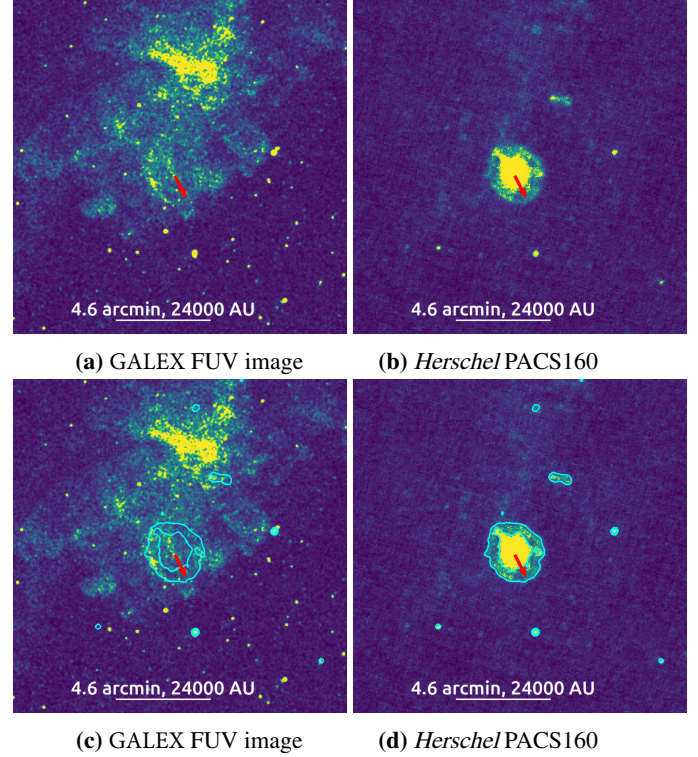


Fig. 5. Extended emission seen around W Hya in FUV (left) and FIR. The emission seen in the IR is cospatial with the arc-like feature seen around the star in the FUV image, marked by the cyan contours (3 and 6σ levels above the background) obtained from the infrared data. The arrows are the same as in Fig. 1.

Despite its low MLR, indications of a bow-shock structure can be seen in the FUV image of TV Psc (Fig. 6a). No IR emission is present, but the NUV emission is rather strong. It is most likely associated with the star itself, being seen as a fairly pronounced circular shape around it (Fig. 6b). Although it is the smallest extended structure presented in this paper (located only $\approx 6600 \text{ AU}$ from the star and corresponding to a kinematic age of 3100 yr , assuming a gas expansion velocity of 10 km s^{-1}), the position of FUV emission correlates well with TV Psc's direction of motion. This correlation and the shape of the structure point to this being an effect of wind-ISM interaction, supported by the fact that the space velocity we computed (78 km s^{-1}) is almost an order of magnitude higher than the assumed outflow velocity (10 km s^{-1}), indicating that shocks are indeed the most likely culprit for the FUV emission in this case. A fairly pronounced and extended halo is seen in the NUV (and partly in the FUV), suggesting some other mechanism might be at play here. Its extent is given by the 1σ level shown in Fig. 6d, after which it drops in intensity significantly. This could be fluorescence caused by a companion, but the available data are not sufficient for a clear conclusion.

3.6. RZ Sagittarii

The only S-type star in the sample, RZ Sgr, is a Mira-type variable and is located approximately 432 pc away. Parameters gathered from the literature suggest that it is in a relatively advanced evolutionary stage on the AGB branch. It has an effective temperature of 2400 K (Schöier et al. 2013), a luminosity of

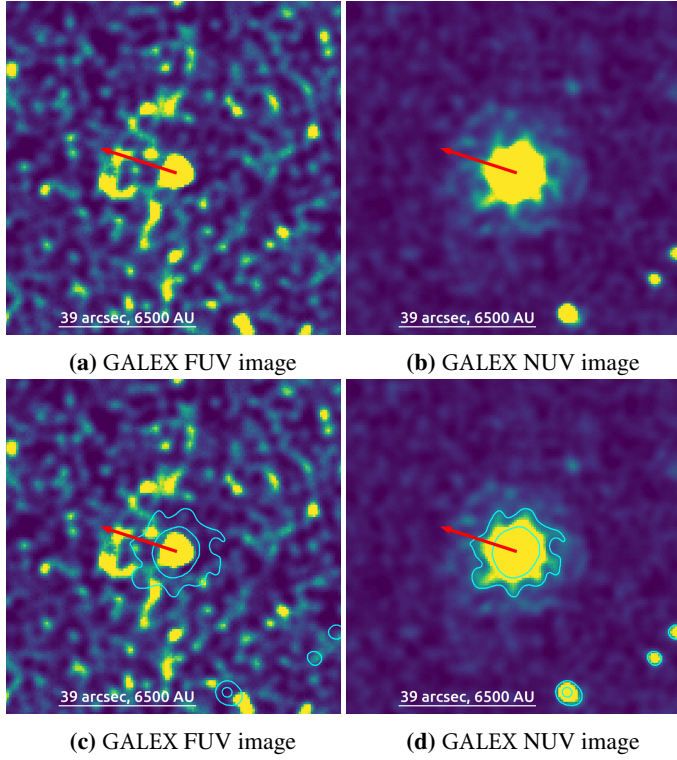


Fig. 6. Extended emission seen around TV Psc in FUV (left) and NUV (right). The cyan contours represent the 1 and 3 σ levels of emission above the background in the NUV data. The arrows are the same as in Fig. 1.

5000 L_{\odot} (scaled for the distance computed by Andriantsaralaza et al. 2022 and based on the value of Winters et al. 2003), and a period of approximately 223 days (Samus' et al. 2017).

RZ Sgr has the highest MLR in our sample, of the order of $10^{-6} M_{\odot} \text{ yr}^{-1}$ based on CO line data (Ramstedt et al. 2009). Multiple IRAS studies report it as having an extended structure at 60 and 100 μm (Fouque et al. 1992; Young et al. 1993), and Whitelock (1994) reported some optical nebulosity around the star that might be related to the extended FIR structure. More recently Andriantsaralaza et al. (2021) observed the CSE of RZ Sgr in CO($J=2-1$) and ($J=3-2$) emission, using the Atacama Compact Array. They report an inner CO CSE, with a size of ≈ 6600 AU, which shows signs of anisotropies (mainly towards the north with respect to the star) and even a potential extended spiral structure.

Herschel FIR images of RZ Sgr show some extended emission surrounding the star (see Fig. 7e). The emission has a tentative eye shape, and a potential bipolar outflow can be seen. It is interesting that this FIR emission is cospatial with the central part of the FUV emission seen in Fig. 7a and also with the NUV emission (Fig. 7b). A close inspection of Fig. 7a reveals that the FUV emission covers two different regions: a central part where the FUV emission is stronger and that is also cospatial with the FIR and NUV observations, and a fainter but much more extended ellipsoidal part with some potential asymmetry towards the north. The placement of this star in the IRAS colour-colour diagram (Fig. 2) would support this two-outflow structure as it lies in a region mainly occupied by objects having hot O-rich material separated from more distant cold dust. The studies of Sahai & Liechti (1995) and Jorissen & Knapp (1998) first postulated a two-outflow scenario (one of which is

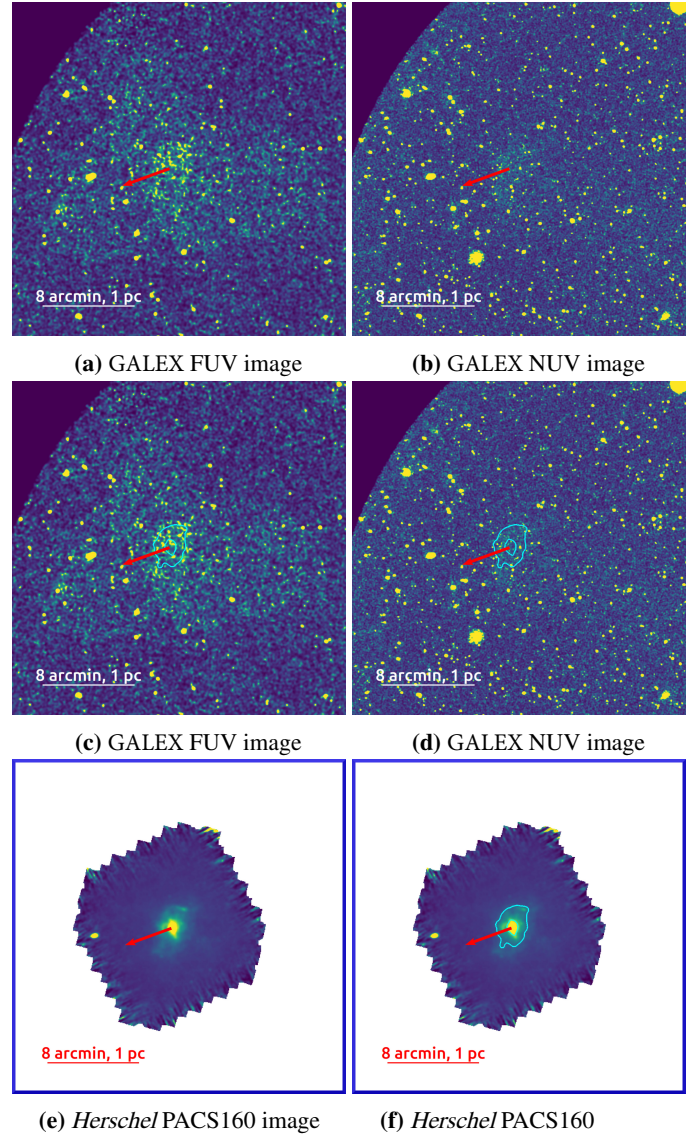


Fig. 7. Extended emission seen around the star RZ Sgr in FUV (panels a and c), NUV (panels b and d), and FIR (panels e and f). The emission seen in the bottom images is cospatial with the more pronounced central emission seen in the GALEX images (FUV and NUV). The cyan contours represent the 2 and 5 σ levels of emission above the background in the FIR data. The arrows are the same as in Fig. 1.

slower) following their CO observations, based on the fact that the expansion velocity derived from the CO($J=2-1$) line was not the same as the one derived from the CO($J=1-0$) line.

Wind-wind or wind-ISM interactions could be the reason for the extended structure seen only in the FUV, considering the space velocity of the star of 41 km s^{-1} . Using a constant gas expansion velocity of 10 km s^{-1} , this structure has an outer radius of as much as $R_{\text{es}} \approx 180\,000$ AU and a kinematic age of 85 000 yr. Targeted observations would be necessary for gathering more information about this very large and faint structure. The origin of the diffuse inner region that is visible in all three wavelength ranges (FUV, NUV, FIR) is unclear.

3.7. DM Tucanae

DM Tuc is another M-type SRb variable. Its MLR, of the order of $10^{-7} M_{\odot} \text{ yr}^{-1}$ (Winters et al. 2003), and other stellar parameters

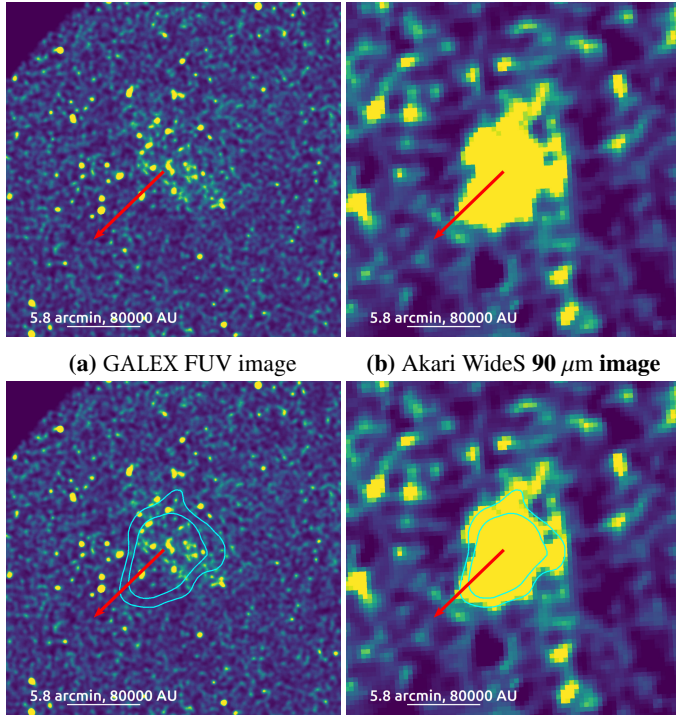


Fig. 8. Extended emission seen around DM Tuc in FUV (left) and FIR (right). The cyan contours represent the 2 and 4 σ levels of emission above the background in the FIR data. The arrows are the same as in Fig. 1.

indicate it is in a more advanced stage of the AGB phase in comparison to β Gru or TV Psc. It is located at a distance of 232 pc and has a variability period of 75 or 145 days (Samus' et al. 2017), which suggests the star is most likely oscillating between two different pulsation modes.

It is not a well-studied object, and little is known about its surroundings. The IRAS colour-colour diagram placement suggests DM Tuc could have a thin O-type CSE. Akari FIR observations support this (see Fig. 8b); the 90 μ m image shows some extended emission around the star. This emission is also partially cospatial with the irregular emission seen in the FUV observations (Fig. 8a). Figure 8 reveals that both the FUV and FIR irregular structures span a similar size, of the order of a few 10^4 AU. What makes this case more interesting is the orientation of the emission. While the FUV emission seems to be oriented NE–SW, the FIR emission is oriented more along a NW–SE axis. Once more the FUV emission appears clumpy. The computed space velocity of the star is almost an order of magnitude higher than the assumed outflow velocity (87 vs. 10 km s $^{-1}$), suggesting that shocked H_2 could be a plausible source of emission.

3.8. V420 Vulpeculae

V420 Vul is a C-type Mira variable located about 2429 pc away. Apart from its variability period of 377 days (Samus' et al. 2017), little is known about it. Using the radiative transfer code *More of DUSTY* (Groenewegen 2012) we calculated its effective temperature, luminosity, and present-day ML to be approximately $T_{\text{eff}} = 3000$ K, $L = 4000 L_{\odot}$, and $\dot{M}_{\text{pd}} = 1.7 \times 10^{-7} M_{\odot} \text{ yr}^{-1}$, respectively.

Some extended emission is present around it in the FUV, but it is very faint and irregular. However, it is in the same region where extended FIR emission can be observed (see Fig. 9).

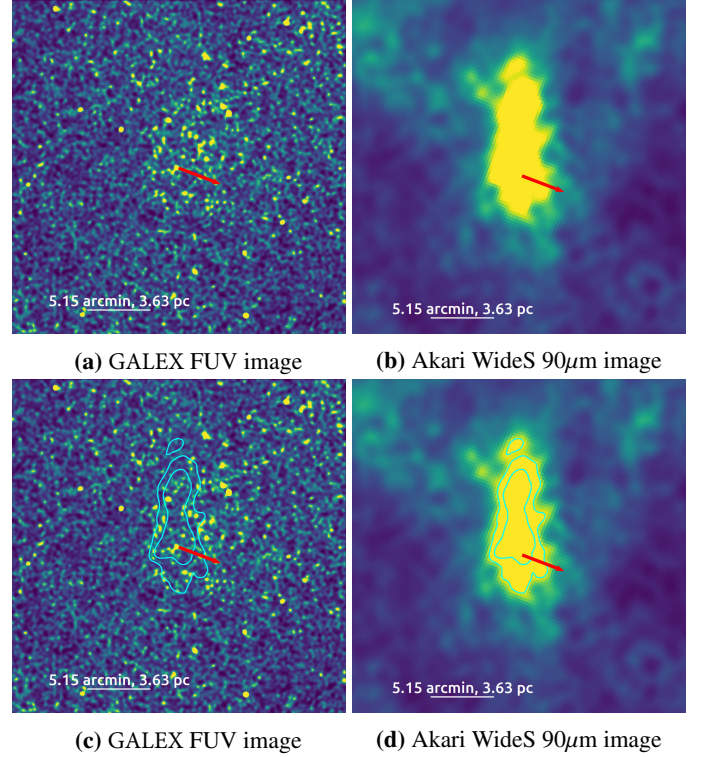


Fig. 9. Extended emission seen around V420 Vul in FUV (left) and FIR (right). The cyan contours represent the 3 and 4 σ levels of emission above the background in the FIR data. The arrows are the same as in Fig. 1.

There is no obvious correlation between the proper motion of the star and the FUV emission. The computed space velocity of 132 km s $^{-1}$ is more than an order of magnitude higher than the assumed 10 km s $^{-1}$ outflow velocity. Combined with the apparent clumpiness of the FUV emission this suggests that the shocked molecular hydrogen scenario proposed by Sanchez et al. (2015) could apply.

4. Discussion and summary

This paper presents a short analysis of a few AGB stars that display extended emission in the FUV: five M-type, two C-type, and one S-type. The sources were identified based on the General Catalogue of Variable Stars, meaning there is a bias towards optically bright, and hence low-MLR AGB stars in this survey. In six cases the FUV emission was found to be cospatial with previous IR detections of extended emission. In three cases the FUV emission is seen in the form of circular shells centred on the stars, and in one of these cases the emission is clearly brighter in the direction of motion of the star.

With the exception of two objects, no NUV emission (0.18 – 0.28 μ m) is seen around the sample stars. This aspect rules out a few emission mechanisms, such as dust-scattering. One of the remaining possible processes in this case is related to shocks, most likely in the form of line emission from shock-excited H_2 , which is produced via the interaction of molecular hydrogen, originating in the cool wind, with hot electrons coming from the post-shock gas (e.g. Martin et al. 2007; Sahai & Chronopoulos 2010; Sahai & Mack-Crane 2014). In these instances there would be no NUV counterpart, which is observed in most of the cases presented here. With the exception of one object (β Gru), all stars

have computed space velocities of 40 km s^{-1} or more (Table 2), indicating that they are moving quite fast through the surrounding ISM. These high velocities are an additional argument in favour of the shock scenario, as temperatures that are high enough to shift the flux of the emission of the outflows towards the UV regime cannot otherwise be produced in the interaction and/or post-shock regions. It is also suggested that such emission would show up in clumps (Sanchez et al. 2015), an aspect that is visible in some of the cases presented above. The relatively short exposure time of the UV data could be the reason for the observed clumpiness, however, so deeper observations would be necessary to determine if this is a potential indicator of this type of FUV emission. For the cases with NUV emission or a diffuse morphology it is unclear what the origin of the UV emission is.

The objects presented here increase the number of known AGB stars that display some type of UV emission. While this sample is by no means significant enough, we note that FUV emission seems to be capable of tracing large old ML structures that are otherwise too faint to be seen in the IR. This transition can already be seen in the cases of R Dor and U Ant, where the IR emission of the large shells is starting to be fairly faint, both shells having a kinematic age of more than 15 000 yr. In the case of β Gru, whose shell has a kinematic age of 27 500 yr, there is no trace of IR emission.

While the UV wavelength regime has been used to observe AGB stars, extended and high-resolution observations are few in number. If the conclusions above hold, future UV studies focused on AGB stars could provide valuable information regarding stellar evolution and the enrichment of the interstellar medium.

Acknowledgements. This publication is based on data acquired with the Atacama Pathfinder Experiment (APEX) under programme ID [O-0109.F-9314A]. APEX is a collaboration between the Max-Planck-Institut für Radioastronomie, the European Southern Observatory, and the Onsala Space Observatory. Swedish observations on APEX are supported through Swedish Research Council grant No 2017-00648.

References

- Andriantsaralaza, M., Ramstedt, S., Vlemmings, W. H. T., et al. 2021, *A&A*, **653**, A53
- Andriantsaralaza, M., Ramstedt, S., Vlemmings, W. H. T., & De Beck, E. 2022, *A&A*, **667**, A74
- Aringer, B., Girardi, L., Nowotny, W., Marigo, P., & Bressan, A. 2016, *MNRAS*, **457**, 3611
- Aringer, B., Marigo, P., Nowotny, W., et al. 2019, *MNRAS*, **487**, 2133
- Bedding, T. R., Zijlstra, A. A., Jones, A., & Foster, G. 1998, *MNRAS*, **301**, 1073
- Bianchi, L., Shiao, B., & Thilker, D. 2017, *ApJS*, **230**, 24
- Cox, N. L. J., Kerschbaum, F., van Marle, A. J., et al. 2012, *A&A*, **537**, A35
- Decin, L., Montargès, M., Richards, A. M. S., et al. 2020, *Science*, **369**, 1497
- Engelke, C. W., Price, S. D., & Kraemer, K. E. 2006, *AJ*, **132**, 1445
- Everett, W. B., Zhang, L., Crawford, T. M., et al. 2020, *ApJ*, **900**, 55
- Famaey, B., Pourbaix, D., Frankowski, A., et al. 2009, VizieR Online Data Catalog: *J/A+A/498/627*
- Fesen, R. A., Drechsler, M., Weil, K. E., et al. 2021, *ApJ*, **920**, 90
- Fouque, P., Le Bertre, T., Epchtein, N., Guglielmo, F., & Kerschbaum, F. 1992, *A&AS*, **93**, 151
- Gaia Collaboration 2018, VizieR Online Data Catalog: *I/345*
- Gaia Collaboration 2022, VizieR Online Data Catalog: *I/355*
- Gontcharov, G. A. 2006, *Astron. Astrophys. Transac.*, **25**, 145
- Groenewegen, M. A. T. 2012, *A&A*, **543**, A36
- Güsten, R., Nyman, L. Å., Schilke, P., et al. 2006, *A&A*, **454**, L13
- Hawkins, G. W. 1990, *A&A*, **229**, L5
- Herwig, F. 2005, *ARA&A*, **43**, 435
- Hoai, D. T., Tuyet Nhung, P., Darriulat, P., et al. 2022, *Vietnam J. Sci. Technol. Eng.*, **64**, 16
- Höfner, S., & Olofsson, H. 2018, *A&ARv*, **26**, 1
- Izumiura, H., Waters, L. B. F. M., de Jong, T., et al. 1997, *A&A*, **323**, 449
- Jorissen, A., & Knapp, G. R. 1998, *A&AS*, **129**, 363
- Judge, P. G. 1986, *MNRAS*, **223**, 239
- Kerschbaum, F., Mecina, M., Ottensamer, R., et al. 2011, *ASP Conf. Ser.*, **445**, 589
- Kerschbaum, F., Maercker, M., Brunner, M., et al. 2017, *A&A*, **605**, A116
- Khoury, T., de Koter, A., Decin, L., et al. 2014, *A&A*, **561**, A5
- Kimeswenger, S., Thorstensen, J. R., Fesen, R. A., et al. 2021, *A&A*, **656**, A145
- Maercker, M., Olofsson, H., Eriksson, K., Gustafsson, B., & Schöier, F. L. 2010, *A&A*, **511**, A37
- Maercker, M., Mohamed, S., Vlemmings, W. H. T., et al. 2012, *Nature*, **490**, 232
- Maercker, M., Danilovich, T., Olofsson, H., et al. 2016, *A&A*, **591**, A44
- Maercker, M., Khouri, T., De Beck, E., et al. 2018, *A&A*, **620**, A106
- Martin, D. C., Seibert, M., Neill, J. D., et al. 2007, *Nature*, **448**, 780
- Massalkhi, S., Agúndez, M., Cernicharo, J., & Velilla-Prieto, L. 2020, *A&A*, **641**, A57
- Muller, S., Dinh-V-Trung, H., J.-H., & Lim, J. 2008, *ApJ*, **684**, L33
- Murphy, T., Sadler, E. M., Ekers, R. D., et al. 2010, *MNRAS*, **402**, 2403
- Ohnaka, K., Weigelt, G., & Hofmann, K.-H. 2019, *ApJ*, **883**, 89
- Olofsson, H., Eriksson, K., & Gustafsson, B. 1988, *A&A*, **196**, L1
- Ortiz, R., & Guerrero, M. A. 2023, *MNRAS*, **522**, 811
- Otero, S. A., & Moon, T. 2006, *JAAVSO*, **34**, 156
- Ramstedt, S., & Olofsson, H. 2014, *A&A*, **566**, A145
- Ramstedt, S., Schöier, F. L., Olofsson, H., & Lundgren, A. A. 2008, *A&A*, **487**, 645
- Ramstedt, S., Schöier, F. L., & Olofsson, H. 2009, *A&A*, **499**, 515
- Ramstedt, S., Vlemmings, W. H. T., Doan, L., et al. 2020, *A&A*, **640**, A133
- Sahai, R., & Chronopoulos, C. K. 2010, *ApJ*, **711**, L53
- Sahai, R., & Liechti, S. 1995, *A&A*, **293**, 198
- Sahai, R., & Mack-Crane, G. P. 2014, *AJ*, **148**, 74
- Sahai, R., & Stenger, B. 2023, *AJ*, **165**, 229
- Samus', N. N., Kazarovets, E. V., Durlevich, O. V., Kireeva, N. N., & Pastukhova, E. N. 2017, *Astron. Rep.*, **61**, 80
- Sanchez, E., Montez, Rodolfo, J., Ramstedt, S., & Stassun, K. G. 2015, *ApJ*, **798**, L39
- Schneider, R., Valiante, R., Ventura, P., et al. 2014, *MNRAS*, **442**, 1440
- Schöier, F. L., Ramstedt, S., Olofsson, H., et al. 2013, *A&A*, **550**, A78
- Schönrich, R., Binney, J., & Dehnen, W. 2010, *MNRAS*, **403**, 1829
- Sloan, G. C., & Price, S. D. 1998, *ApJS*, **119**, 141
- van der Veen, W. E. C. J., & Habing, H. J. 1988, *A&A*, **194**, 125
- van Leeuwen, F. 2007, *A&A*, **474**, 653
- Vlemmings, W. H. T., Humphreys, E. M. L., & Franco-Hernández, R. 2011, *ApJ*, **728**, 149
- Vlemmings, W. H. T., Khouri, T., De Beck, E., et al. 2018, *A&A*, **613**, L4
- Vogt, N., Contreras-Quijada, A., Fuentes-Morales, I., et al. 2016, *ApJS*, **227**, 6
- Whitelock, P. 1994, *MNRAS*, **270**, L15
- Winters, J. M., Le Bertre, T., Jeong, K. S., Nyman, L. Å., & Epchtein, N. 2003, *A&A*, **409**, 715
- Young, K., Phillips, T. G., & Knapp, G. R. 1993, *ApJ*, **409**, 725

Appendix A: Regions for flux density determination

The data used here are pipeline-calibrated data, using the [GR7 calibration process](#) for U Ant and the [GR6 calibration process](#) for all other objects. Following a by-eye inspection of the FUV images, the regions were manually defined to estimate the FUV flux densities of the extended emission for each object. In the cases where the emission is diffuse, only one region was defined. For those cases where the extended structures were more pronounced, two regions were defined. The flux densities measured for the latter cases are for the area contained between the two green shapes (see Fig. A.1). A small region placed in an area of minimal emission was used in each case to determine the detector background, which was then subtracted from the obtained flux densities, as a simple means of background correction. The flux densities were obtained by converting the photon counts into janskys via the following relation:

$$F_{\text{FUV}} [\text{Jy}] = 1.115 \times 10^{-4} \times \text{cps} [\text{counts/second/pixel}].$$

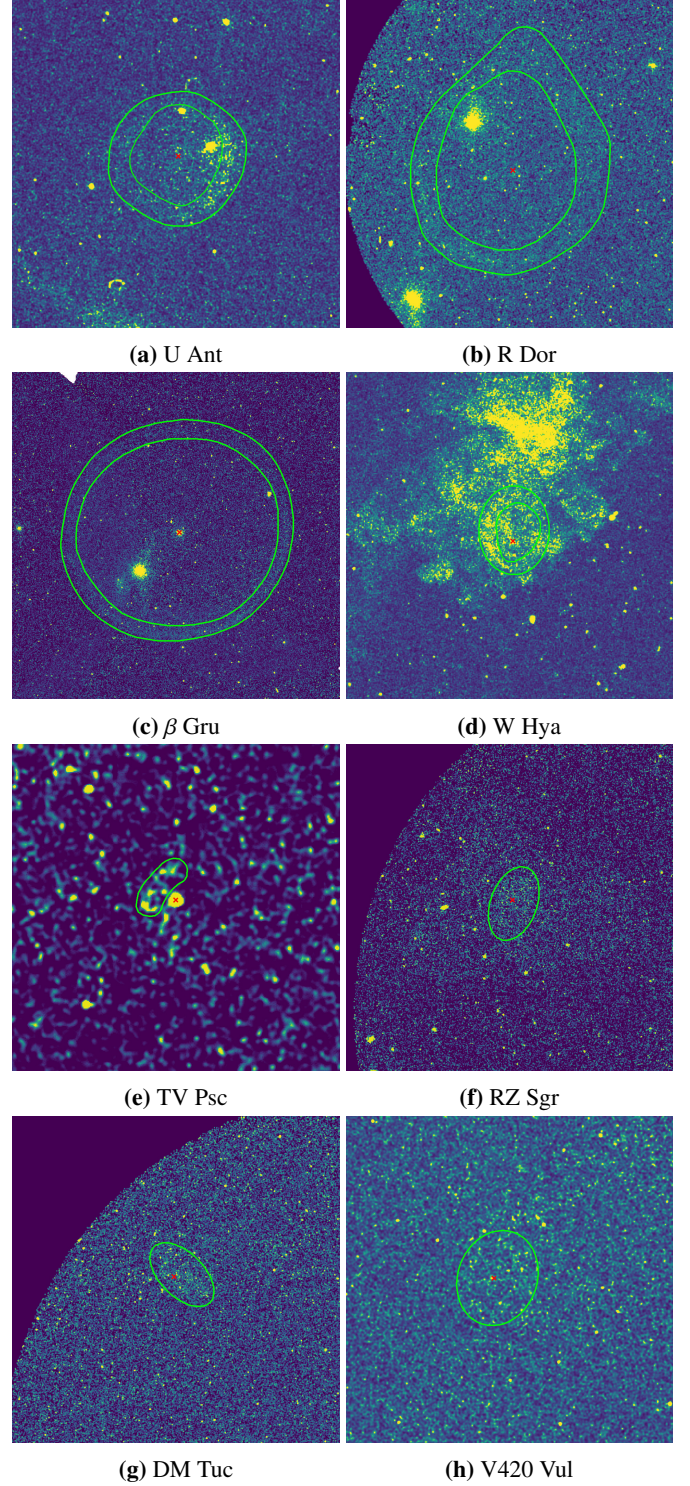


Fig. A.1: Regions used for flux density estimates. In each panel the red cross represents the location of the star.